Pure P- and S-wave elastic reverse time migration with adjoint state method imaging condition

Jorge E. Monsegny* and Daniel O. Trad

ABSTRACT

We implemented an elastic reverse time migration based on a coupled system of pure P- and S-wave particle velocities. The system utilizes finite difference wavefields for P- and S-wave particle velocity in vertical and horizontal directions (v_{px}, v_{pz}, v_{sx} and v_{sz}), and for 2-D displacement divergence and curl (A and B). In contrast with the usual elastic imaging conditions that cross-correlates vertical displacements to obtain the P-wave image and vertical and horizontal displacements to obtain the converted wave image, we devised P- and S-wave imaging conditions using the adjoint state method. The resulting imaging conditions cross-correlate spatial derivatives of A and B wavefields with P- and S-wave displacements. The proposed migration shows a better reflector definition and more balanced amplitudes than the usual vertical and horizontal particle displacement cross-correlations.

INTRODUCTION

Reverse time migration (RTM) is a migration method that uses the two-way wave equation and can cope with primaries, multiples and complex structures with all reflector dips (Baysal et al., 1983; McMechan, 1983; Whitmore, 1983). RTM is usually used to migrate P-wave seismic data using the scalar wave equation, however it can also be used with the elastic wave equation. Sava and Hill (2009) show a tutorial of wave migration methods including RTM.

The basic RTM algorithm is shown in Algorithm 1. The first input is the shot gathers S that could be pressure or vertical displacement in acoustic RTM, or multicomponent seismograms in elastic RTM. The second input is the parameter model $\boldsymbol{m}$ that, for example, in P-wave acoustic RTM is P-wave velocity or Bulk modulus and density. For elastic RTM, $\boldsymbol{m}$ is P- and S-wave velocity or the Lamé parameters and density. The last input is the source wavelet that could be one dimensional in acoustic RTM or multidimensional in elastic RTM.

The outer loop iterates over shot gathers with the final migrations being the stack of each individual migrated shot. Inside this loop, the algorithm generates source and receiver wavefields and calculates some imaging conditions to create the migrated images.

The first step is to calculate the source wavefields doing a forward propagation. Depending on the finite difference scheme various wavefield combinations $\boldsymbol{F}$ are stored. For acoustic RTM they could be particle pressure or the scalar P-wave particle velocity/displacement. For elastic RTM, they could be the Cartesian components of the particle velocity/displacement, the stresses, or the P- and S-wave potentials. Also, there is no need to store the whole wavefields but just the borders and reconstruct them (Nguyen and McMechan, 2015).

The middle loop iterates backward in time generating the receiver wavefields by running the finite difference scheme in reverse with the shot gathers S as input wavelets at receiver positions. There is no need to store the whole wavefields $\boldsymbol{B}$ but just the one corresponding to the current time step.

Finally, the inner loop calculates the imaging conditions based on wavefields $\boldsymbol{F}$ and $\boldsymbol{B}$ (Claerbout, 1971). In acoustic migration they could be as simple as cross-correlating forward and backward pressure wavefields, expecting large amplitudes at reflector positions and destructive interference everywhere else. In the case of elastic RTM, the imaging conditions are more complicated and suffer from various problems.

Data: Shot gathers $S(\boldsymbol{x}, t, i)$ for $i = 1, \ldots, N_s$, parameter models $\boldsymbol{m}$ and source wavelet $s(t)$.
Result: Migrated images $I_w(\boldsymbol{x}), w = 1, \ldots, N_w$.
For each shot gather;
for $s \leftarrow 1$ **to** N_s **do**
  Do a complete forward propagation getting all forward (source) wavefields of interest;
  $\boldsymbol{F} \leftarrow$ `FD(`$\boldsymbol{m}$`,`s`)`;
  Reverse time loop;
  for $t \leftarrow t_{max}$ **to** 0 **do**
    Do one step backwards using shot gathers as sources and getting all backward (receiver) wavefields of interest;
    $\boldsymbol{B} \leftarrow$ `OneStepFD(`$\boldsymbol{m}$`,`$S(:,:,t)$`)`;
    Apply imaging conditions at current time;
    for *each type of imaging condition* **do**
      $I_w(:,:) \leftarrow I_w(:,:) +$ `ImagCond`$_w$`(`$\boldsymbol{F}$`,`$\boldsymbol{B}$`)`;
    end
  end
end

Algorithm 1: Basic reverse time migration algorithm.

Regarding the elastic imaging conditions, there are two main approaches based on what you want to obtain. The first approach, mentioned before, is to cross-correlate the Cartesian components of the particle velocity/displacement (Chang and McMechan, 1994; Jiang, 2012). In two dimensions the obtained migration images are I_{zz}, I_{zx}, I_{xz} and I_{xx} where the first subscript corresponds to the forward wavefield component and the second to the backward. Due to the seismic mode filter characteristics of the near surface, image I_{zz} could be considered akin to a P-wave migration while I_{zx} could be to a PS-wave migration. However, the practice shows that artifacts due to cross-talk between P and S modes are present (Yan and Sava, 2008).

The other approach wants to obtain true PP, PS, SP and SS mode migration images because they have a more physical meaning. Three main paths are identified in the literature. The first one is to propagate separately P- and S-waves (Sun and McMechan, 2001). The

PS image could be calculated using this method by forward propagating the P-wave and backward propagating the S-wave, both acoustically and using its corresponding velocity models. However, the image shows artifacts and wrong amplitudes because there is no conversion between modes.

The second path is to transform the velocity/displacement Cartesian components into P- and S-wave potentials using the Helmholtz decomposition (Yan and Sava, 2008). The main drawbacks are three. The first one is that P- and S-wave amplitude and phase are distorted by the Helmholtz decomposition (Zhang et al., 2018). The second is that S-wave wavefields have a polarity reversal that causes destructive interference when cross-correlated with P-wave wavefields. When the reflector is not horizontal the polarity reversal does not occur at zero offset and this makes it difficult to correct it. This destructive interference produces low amplitude patches in the final PS and SP migrated images (Balch and Erdemir, 1994). Du et al. (2012) solve this issue by calculating a polarity factor along reflectors using the energy flux density vector. Others calculate this factor from poynting vectors (Wang and McMechan, 2015) or by using the normal vector to the reflectors picked from a previous PP migration (Duan and Sava, 2015). The third drawback occurs in three dimensions where the S-wave potential has three components while the P-wave potential only have one. It is not obvious how to generate single PS, SP and SS images by combining a vector and a scalar field. Duan and Sava (2015) calculate the gradient of P-wave potential and the curl of the S-wave potential and use a dot product with the interface normal vectors. On the other hand, Rocha et al. (2016) use the energy norm to obtain a single image for PS and SP converted migration.

The third path is to use a finite difference scheme that directly propagates P- and S-waves. Some of such schemes are Ma and Zhu (2003) and Chen (2014). These schemes preserve the P- and S-wave modes amplitude and phase (Duan and Sava, 2015). Gu et al. (2015) use a similar scheme to calculate P- and S-wave vertical and horizontal displacements and then cross-correlates corresponding wavefields, i.e. forward horizontal P-wave with backward horizontal P-wave. However, they do not cross-correlate different modes to obtain PS images or generate a single image for each mode. Du et al. (2017) aim to obtain a single image by using dot product instead of multiplication in the wavefield cross-correlations. Using this method, they avoid rather than correct the PS and SP polarity reversal. However, the dot product implicitly multiplies by $\cos 2\alpha$ with α being the incident angle and this generates polarity reversal in PP and SS reflections when they are more than 90° apart.

For least squares RTM the adjoint state method is used to get the gradient of an objective function that uses Born modelling (Schuster, 2017). This gradient is a migration operator adjoint of the Born modelling operator. Zhu et al. (2009) use the adjoint state method to invert for Lamé parameters and density using full waveform inversion (FWI) and then combine these parameters to obtain the contrast between elastic impedances where the reflectors are located. Alves and Biondi (2016) also uses the adjoint state method to obtain multi-parameter RTM images not of PP or PS reflectivities but of Lamé moduli and density that can be applied for structural interpretation.

In this report we use the adjoint state method and the pure P- and S-wave finite difference method of Chen (2014) to obtain elastic migration operators that generate P- and S-wave migrated images. The mentioned finite difference scheme also produces P- and S-wave vertical and horizontal displacements that are combined to generate PP and PS migrations.

The outline of the report is the following: first we describe the pure P- and S-wave finite difference method, highlighting some of its properties. Next, we describe some elastic imaging conditions that can be applied to the usual finite difference method (Levander, 1988) and the pure P- and S-wave one, including the imaging conditions derived with the adjoint state method. Then we perform some numerical experiments showing the effect of each imaging condition described earlier over a single shot gather and a simple velocity model. The other numerical experiments involve applying all the imaging conditions to the elastic Marmousi model (Versteeg, 1994). We follow with a discussion and a conclusion section. Finally, the appendix includes the derivation of the adjoint state imaging conditions and their extension to 3-D.

P- AND S-WAVE ELASTIC RTM

Finite difference scheme

The elastic RTM migration is based on the pure P- and S-wave finite difference system of Chen (2014):

$$
\begin{aligned}
v_x = \frac{\partial u}{\partial t} \qquad & v_z = \frac{\partial w}{\partial t} \\
v_x = v_{px} + v_{sx} \qquad & v_z = v_{pz} + v_{sz} \\
\frac{\partial v_{px}}{\partial t} = \alpha^2 \frac{\partial A}{\partial x} \qquad & \frac{\partial v_{pz}}{\partial t} = \alpha^2 \frac{\partial A}{\partial z} \\
\frac{\partial v_{sp}}{\partial t} = \beta^2 \frac{\partial B}{\partial z} \qquad & \frac{\partial v_{sz}}{\partial t} = -\beta^2 \frac{\partial B}{\partial x} \\
A = \frac{\partial u}{\partial x} + \frac{\partial w}{\partial z} \qquad & B = \frac{\partial u}{\partial z} - \frac{\partial w}{\partial z} \\
\frac{\partial A}{\partial t} = \frac{\partial v_x}{\partial x} + \frac{\partial v_z}{\partial z} + f_A \qquad & \frac{\partial B}{\partial t} = \frac{\partial v_x}{\partial z} - \frac{\partial v_z}{\partial x} + f_B.
\end{aligned}
\tag{1}
$$

In this system u and w are the horizontal and vertical particle displacements while v_x and v_z are their time derivatives or particle velocities. However, the system splits these velocities in their P- and S-wave components v_{px}, v_{pz}, v_{sx} and v_{sz} to explicitly evolve them. The wavefields A and B are the divergence and second curl component of the vector $(u, 0, w)$. Although not explicitly addressed by Chen (2014), the P-wave source f_A and S-wave source f_B are injected to wavefields A and B, respectively. Finally, α and β are the P- and S-wave velocities. Density does not appear explicitly but in combination with Lamé moduli in both of these velocities.

It is important to say that this system simulates the coupled P- and S-wave propagation.

This means that conversions between modes are possible. For example, when a P-wave propagates, it is entirely contained in the P-wave wavefields v_{px}, v_{pz} and A. When it reaches an interface, the reflected and transmitted S-waves appear in the S-wave wavefields v_{sx}, v_{sz} and B.

The system was implemented with a staggered grid and perfectly matched layer boundary conditions Berenger (1994). All the details are in Chen (2014).

We perform two experiments, one using a pure P-wave source with $f_B = 0$ and the other with a pure S-wave source with $f_A = 0$. The model is homogeneous with $\alpha = 2km/s$ and $\beta = 1.15km/s$. The source is in the centre of the model. Figure 1 shows a snapshot of the six wave fields at $0.25s$. Without interfaces to do mode conversions, there is no S-waves. On the other hand, Figure 2 displays the case for the S-wave source. There is no P-waves, only S-waves.

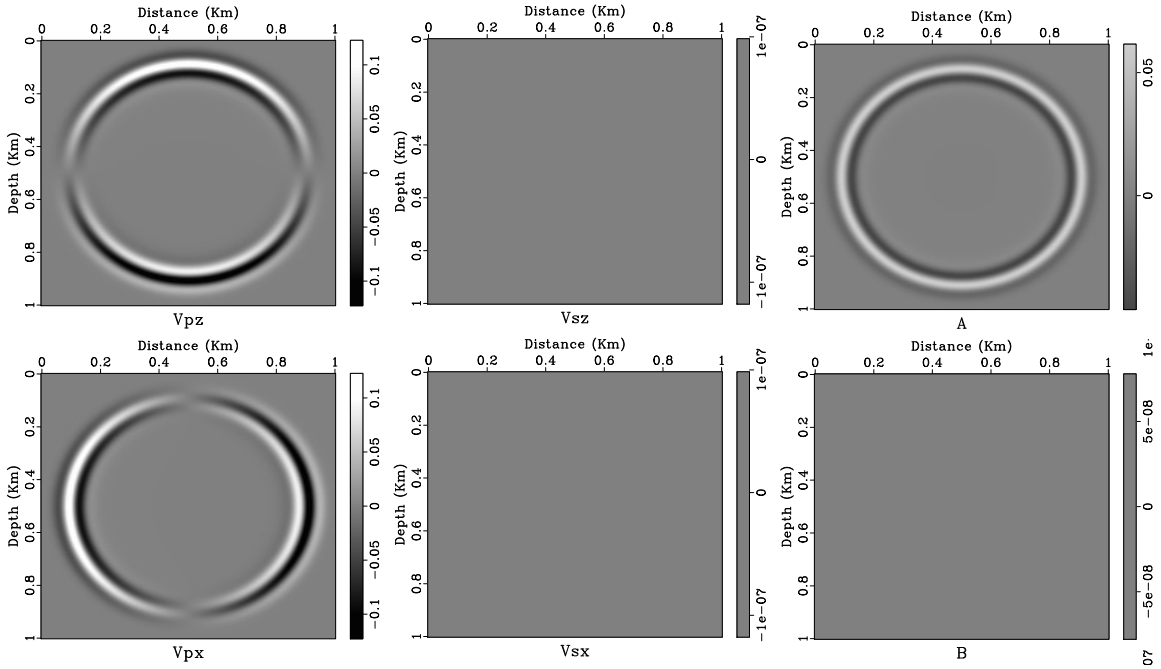

FIG. 1. Wavefield snapshots at $0.25s$ in a homogeneous medium using a P-wave source. As there are no velocity contrasts, there are no mode conversions and the S-wave wavefields are void.

Something that we want to discuss before going to the elastic RTM imaging conditions is the symmetry difference between a P-wave and a S-wave. In the left part of Figure 3 are two schematic diagrams of a P-wave source and the particle movement. The source is in the centre (star). The arrows around show the particle displacement direction that is radial. Four multicomponent geophones are located at the corners (inverted triangles). Above each one of them are the directions of the horizontal and vertical displacements they record at their locations. The centre and right parts of the figure show some snapshots. On one hand, the two P-wave vertical snapshots on the top show a vertical asymmetry of the particle displacement. On the other hand, the other two P-wave horizontal snapshots at the bottom show a horizontal asymmetry. This asymmetry is what changes the polarity in seismogram radial components.

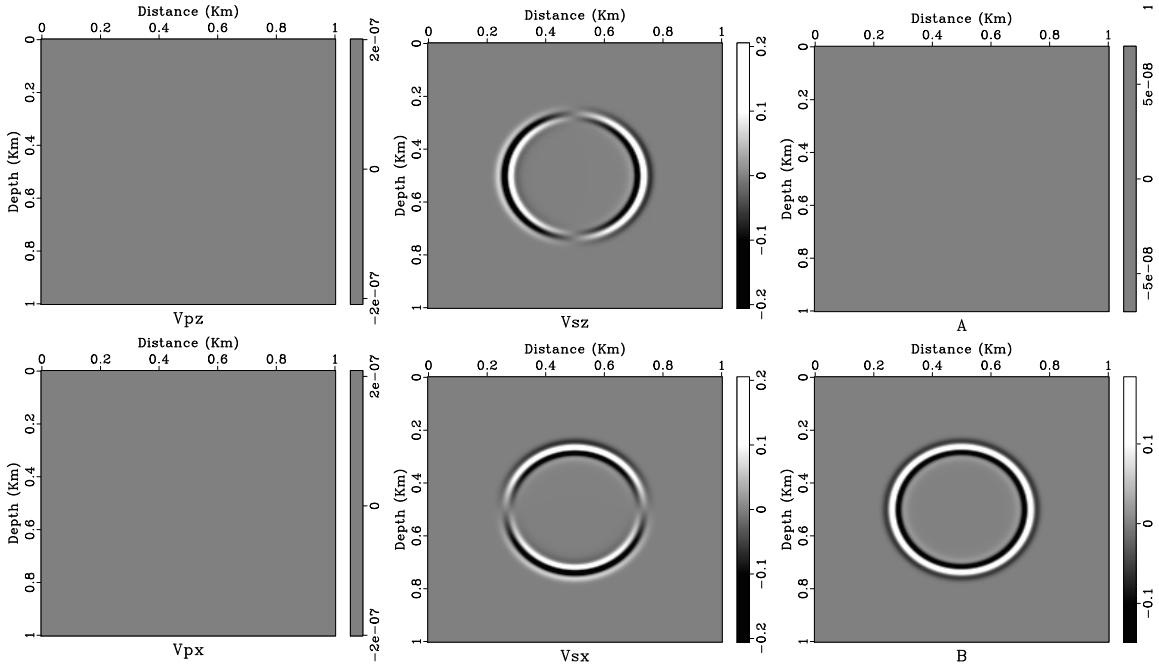

FIG. 2. Wavefield snapshots at $0.25s$ in a homogeneous medium using a S-wave source. Due that there are no velocity contrasts, there are no mode conversions and the P-wave wavefields remain empty.

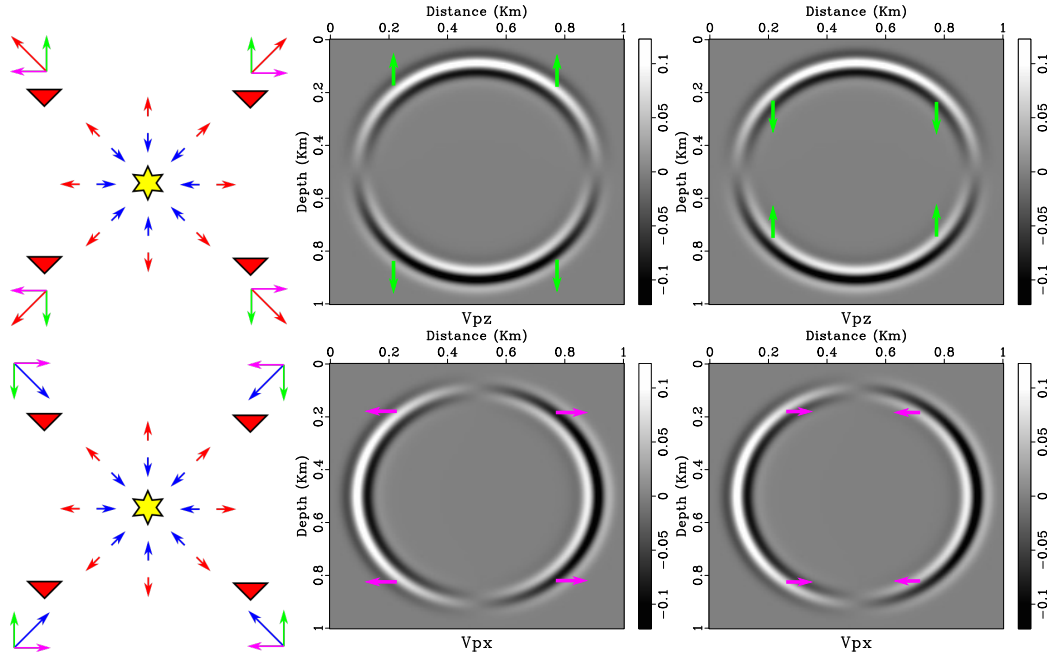

FIG. 3. P-wave source perceived polarity. The diagrams in the left show a P-wave source in the centre (star) and four receivers (inverted triangles) at the corners. Arrows show particle displacement/velocity direction. Above each receiver are the particle directions they record. In the centre and left the wavefield snapshots show that the P-wave vertical snapshots are vertically asymmetrical while horizontal snapshots are horizontally asymmetrical. Arrow colors over the wavefields correspond to arrows in left diagrams.

But something different happens when the source is S-wave. Figure 4 exhibits this case. As before, in the left part appear the schematic diagrams of the S-wave source at

the centre and the particle displacement that now is tangential. The geophones are located at the corners and the particle displacement directions are shown above each one of them. The top S-wave vertical velocity snapshots show that there is horizontal asymmetry while the bottom S-wave horizontal velocity snapshots show that there is a vertical one. This is different from the P-wave source case and due to this we can expect a polarity reversal in the seismogram vertical component instead of the radial.

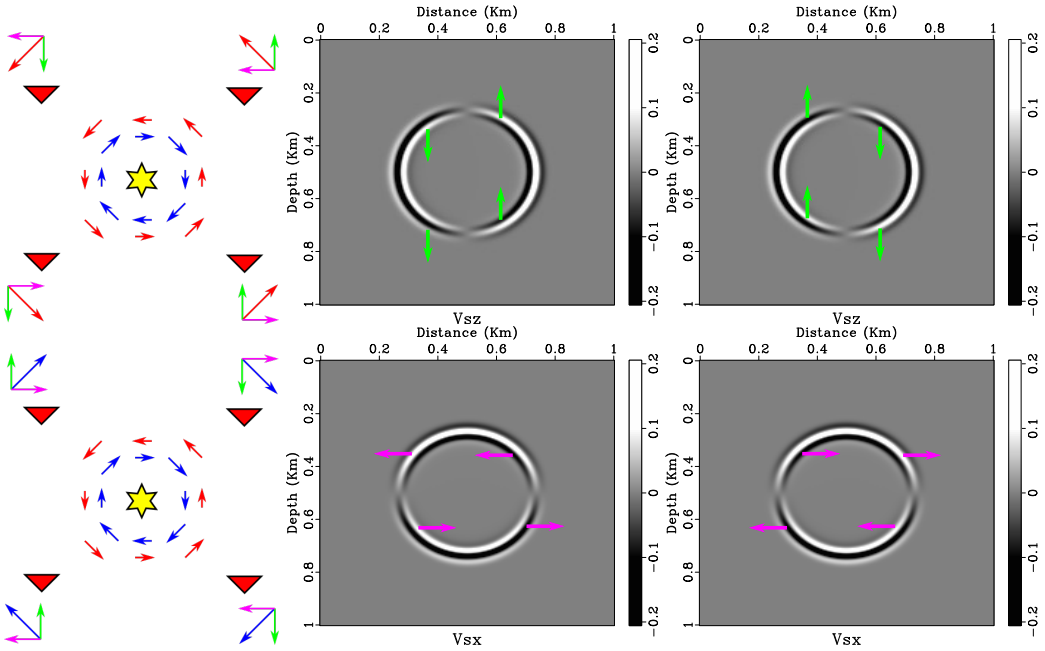

FIG. 4. S-wave source perceived polarity. The diagrams in the left show a S-wave source in the centre (star) and four receivers (inverted triangles) at the corners. Arrows show particle displacement/velocity direction. Above each receiver are the particle directions they record. In the centre and left the wavefield snapshots show that the S-wave vertical snapshots are horizontally asymmetrical while horizontal snapshots are vertically asymmetrical. Arrow colors over the wavefields correspond to arrows in left diagrams.

Figure 6 shows an example with PS conversions in the three-layer model from Figure 5. The three top snapshots correspond to A and the three bottom to B. As the source is P-wave there is direct wave in the first A snapshot but not on the first of B. In the remaining A snapshots we see reflections and transmissions. The last two B snapshots show S-waves created by PS conversions.

Elastic imaging conditions

Acoustic imaging is scalar and its usual imaging condition is to cross-correlate forward and backward pressure wavefields. In contrast, as elastic imaging is vectorial, the choice of how to combine forward and backward wavefields is less obvious.

We would like to compare the pure P- and S-wave imaging conditions with those proposed for RTM with systems that do not distinguish between pure modes like Levander (1988). This system has vertical v_z and horizontal v_z particle velocities in addition to normal and shear stresses σ_{xx}, σ_{zz} and σ_{xz}. One option for imaging conditions is to take

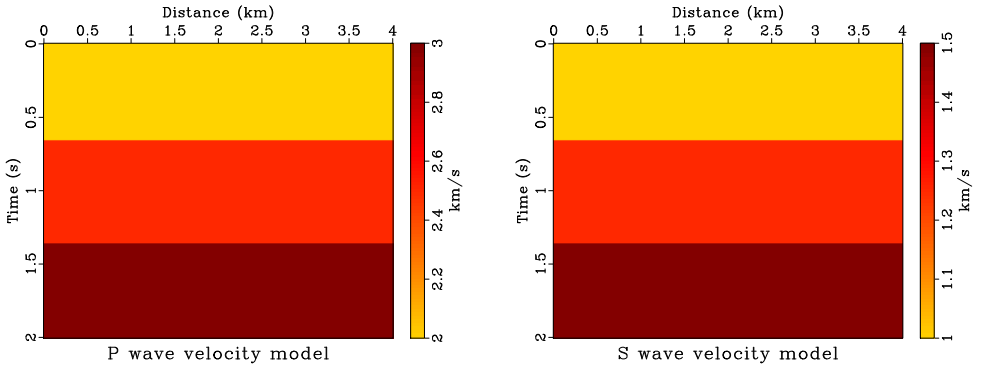

FIG. 5. Three layer P- and S-wave velocity models used in the numerical experiments.

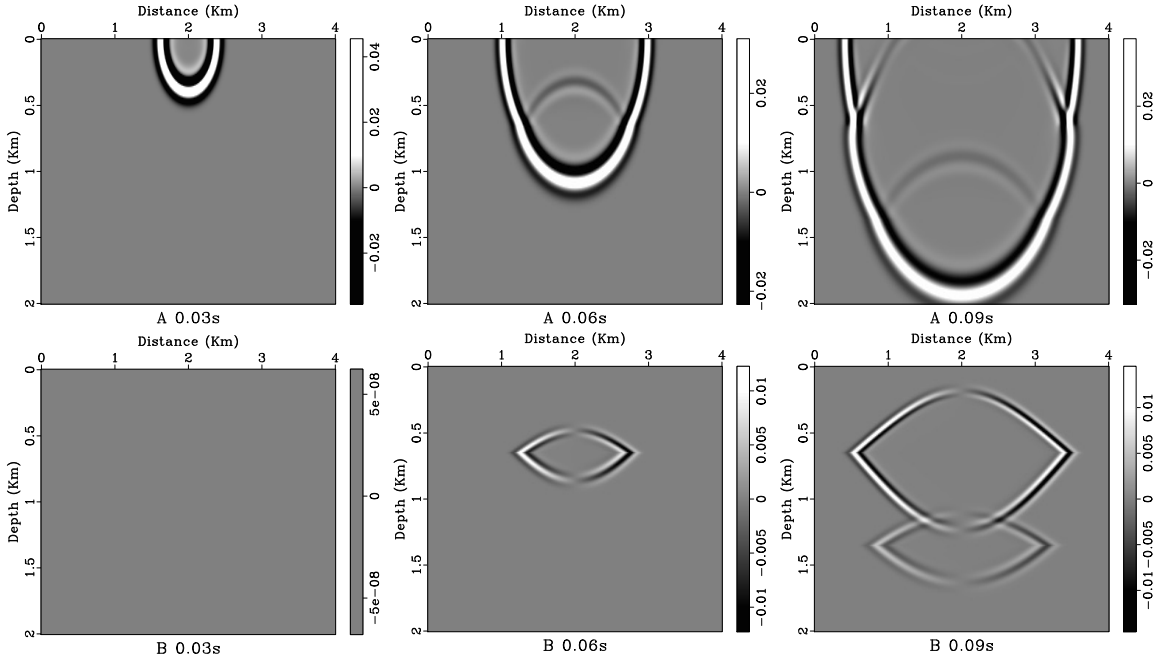

FIG. 6. A and B snapshots at several times. The source is P-wave. In snapshots A appear the direct wave and the P-wave reflections and transmissions. In snapshots B only appear converted S-wave reflections and transmissions.

advantage of the near surface that works as a mode filter by making the P-waves almost vertical and the S-waves almost horizontal with the following two equations for PP and PS (Chang and McMechan, 1994; Jiang, 2012):

$$I_{PP} = \int_0^T v_z \hat{v}_z dt \tag{2}$$

$$I_{PS} = \int_0^T v_z \hat{v}_x dt \tag{3}$$

where T is the maximum seismogram time and the hat ("$\hat{}$") means reverse propagated. Another option to image PP is to cross-correlate the sum or normal stresses relating this sum to the P-wave propagation:

$$I_{PP} = \int_0^T (\sigma_{xx} + \sigma_{zz})(\hat{\sigma}_{xx} + \hat{\sigma}_{zz})dt. \tag{4}$$

Helmholtz decomposition is applied to the particle velocities using divergence $\nabla\cdot$ and curl $\nabla\times$ operators to obtain the P- and S-wave wavefields. Those wavefields are combined in two PP and PS imaging conditions (Yan and Sava, 2008):

$$I_{PP} = \int_0^T \nabla\cdot(v_x, v_z)\nabla\cdot(\hat{v}_x, \hat{v}_z)dt \tag{5}$$

$$I_{PS} = \int_0^T \nabla\cdot(v_x, v_z)(\nabla\times(\hat{v}_x, 0, \hat{v}_z))_2 dt \tag{6}$$

where we use the 2D curl operator by extending the particle velocity vector and using only the second component. However, this PS imaging condition using Helmholtz decomposition does not translate directly to 3D because the result of curl operator is a vector while the divergence is still a scalar.

Regarding the P- and S-wave pure mode system, there are also several imaging conditions. Du et al. (2017) propose to perform the dot product between the Cartesian components of the P and S modes to obtain two PP and PS imaging conditions:

$$I_{PP} = \int_0^T (v_{px}, v_{pz})\cdot(\hat{v}_{px}, \hat{v}_{pz})dt \tag{7}$$

$$I_{PS} = \int_0^T (v_{px}, v_{pz})\cdot(\hat{v}_{sx}, \hat{v}_{sz})dt. \tag{8}$$

The interpretation of these imaging conditions is that they calculate the projection of the source wavefield into the receiver wavefield. However, Du et al. (2017) use a different finite difference system than us. In our system we identify the wavefield A with the displacement divergence and B with the displacement curl. Another imaging condition is to cross-correlate these two wavefields:

$$I_{PS} = \int_0^T A\hat{B}dt. \tag{9}$$

Finally, we propose two imaging conditions for PP and PS that are obtained by the adjoint state method (Feng and Schuster, 2017). Their derivations and 3D extension are in the appendix:

$$I_{PP} = 2\alpha \int_0^T \left(\frac{\partial A}{\partial x}, \frac{\partial A}{\partial z} \right) \cdot (\hat{v}_{px}, \hat{v}_{pz}) dt \quad (10)$$

$$I_{PS} = 2\beta \int_0^T \left(\frac{\partial B}{\partial z}, -\frac{\partial B}{\partial x} \right) \cdot (\hat{v}_{sx}, \hat{v}_{sz}) dt. \quad (11)$$

In these dot products the backpropagated wavefields are the Cartesian components of particle velocities, while the forward propagated wavefields are spatial derivatives of A and B. The imaging condition also multiplies the cross-correlation by twice the corresponding velocity.

As several authors have suggested, to correct for uneven illumination a division by the source or source plus receiver energy could make the migration results more balanced (Chang and McMechan, 1994; Jiang, 2012). In the non-pure mode RTM we divide by:

$$\int_0^T (v_x^2 + v_z^2) dt$$

and in the pure mode RTM imaging conditions by:

$$\int_0^T (A^2 + B^2) dt.$$

NUMERICAL EXPERIMENTS

We performed several numerical experiments to evaluate the different elastic imaging conditions described in the previous section. The experiments are segregated in two sets. The first one corresponds to equations 2-6 when there is no mode separation in the wave simulation. The second set corresponds to equations 7-11 when there is mode separation. All the images have a Laplacian filter applied to attenuate the low wavenumber noise that is common in RTM images. No AGC or vertical gain were applied.

The first experiment used the three layer velocity models shown before in Figure 5. A single source located in the top centre of the model was shot with receivers along all the surface extension. The source was a stress source, i.e. the same wavelet is injected in the normal stresses wavefields, when there is no mode separation. With mode separation a pure P-wave source was used. In this first experiment the source was a Ricker wavelet with dominant frequency of 12Hz.

Figure 7 displays the migrated results without mode separation using the imaging conditions of equations 2-6. Top row corresponds to the PP images and bottom row to the PS

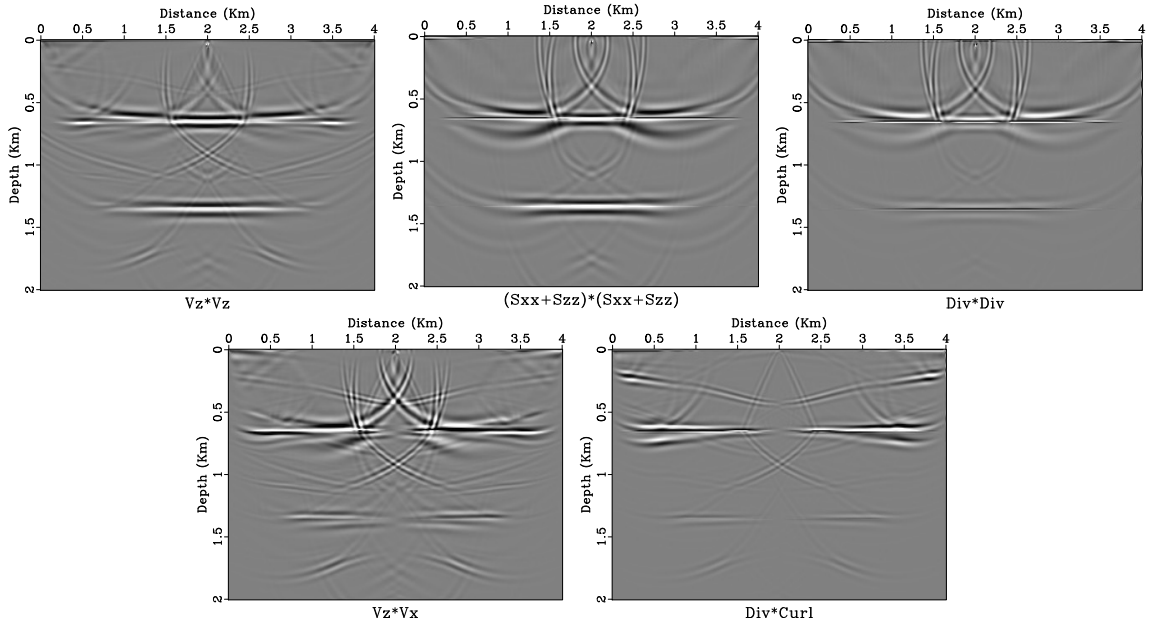

FIG. 7. PP and PS RTM migration results without mode separation. Imaging conditions are those of equations 2-6. Top row are PP imaging conditions and bottom one are PS imaging conditions. From top to bottom and left to right they are vertical displacements, sum of normal stresses, divergence, vertical and horizontal displacement, and divergence times curl.

images. Overall the images show noise due to the source and to crosstalk between different modes. The PP images delineate the reflectors in the central part of the model where the PP reflections are expected to happen. PS images delineate longer reflectors as the conversion points tend to be closer to the receiver than to the source. They also show low amplitudes in the centre due to low S-wave amplitudes close to the normal incidence angle. As expected, the two PS images, VzVx and Div*Curl, exhibit polarity reversal.

Similarly, Figure 8 shows the migrated results with mode separation using image conditions from equations 7-11. As before, top row are PP migrations and bottom row are PS migrations. The PP images show almost no noise related to the crosstalk between modes. The PS on the other hand show spurious events in the bottom part and between the two reflectors. Also, the PS images do not have polarity reversals except for the AB image.

The second experiment uses the elastic Marmousi model (Versteeg, 1994). A total of 17 shots evenly spaced over the model top where simulated with receivers along the top horizontal model extension. In this experiment a 20Hz Ricker wavelet was used as source with and without mode separation.

Figure 9 displays the PP migration results when there is no mode separation. The vertical displacement image shows much less resolution that the sum of normal stresses and divergence images. The sum of stresses tends to show better balance, but the divergence is able to delineate more cleanly the reflectors.

The PS migration results without mode separation appear on Figure 10. Both images show low resolution and very unbalanced amplitudes at the bottom, although the div*curl is

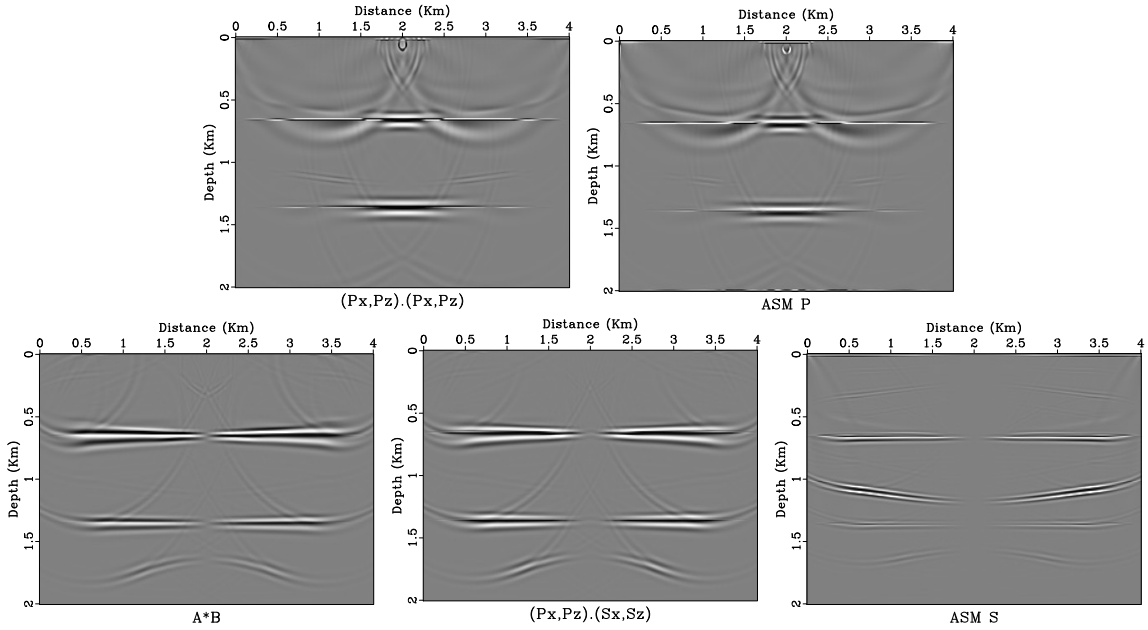

FIG. 8. PP and PS RTM migration results with mode separation. Imaging conditions are those of equations 7-11. Top row are PP imaging conditions and bottom one are PS imaging conditions. From top to bottom and left to right they are P dot product, adjoint state method P, A times B, PS dot product and adjoint state method S.

slightly better. The reason could be the destructive interference caused by polarity reversals and the crosstalk between modes.

Figure 11 exhibits the PP migration results with separation. In both cases the images have good resolution, are able to reconstruct most structures and have good balance. Maybe the dot product one is slightly better than the adjoint state method image because it has less source noise and more continuous reflectors.

Finally, Figure 12 shows the PS migration results with mode separation. The first image, A*B, is not very good. This could be caused because this imaging condition has polarity reversal, and this causes destructive interference that hampers the reflector delineation. The second image is able to do a good reconstruction of most structures and also has a good balance. The last image is better than the first one but not as good as the second. It has too much noise in certain parts and is no capable of reconstruct the intricate structures, just their outlines.

DISCUSSION

The first numerical experiments showed that RTM using pure P- and S-waves generates less artifacts that the usual elastic RTM. In addition, two of the pure PS RTM did not show the polarity reversal typical of those images. All these effects do not make much difference in a single migrated shot but add up in a multishot RTM creating a much better image, like the second numerical experiment exhibits.

The adjoint state method imaging conditions have their origin in the creation of an

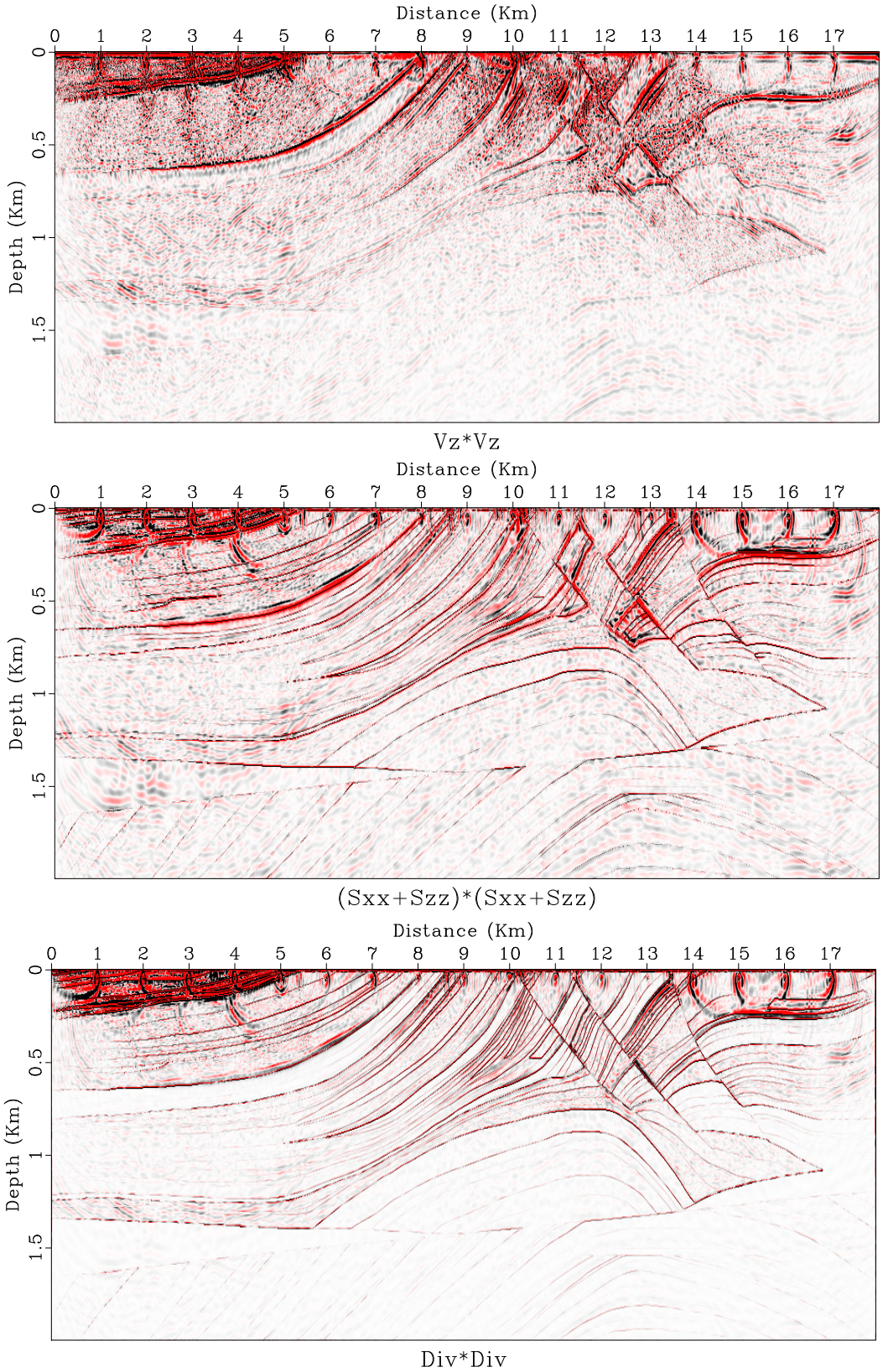

FIG. 9. PP RTM migration results without mode separation. Imaging conditions are those of equations 2, 4 and 5. From top to bottom they are vertical displacements, sum of normal stresses and divergence.

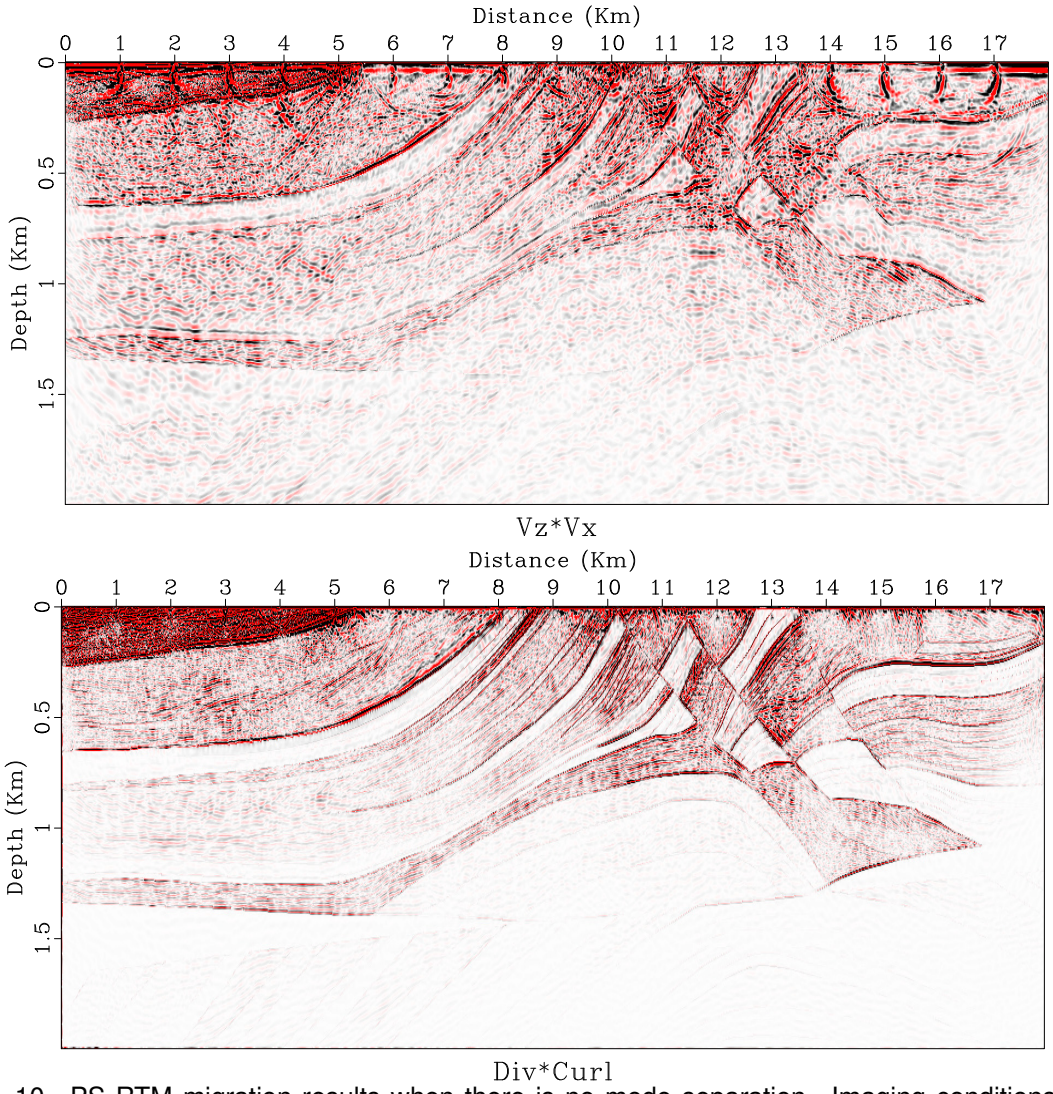

FIG. 10. PS RTM migration results when there is no mode separation. Imaging conditions are those of equations 3 and 6. From top to bottom they are vertical and horizontal displacement, and divergence times curl.

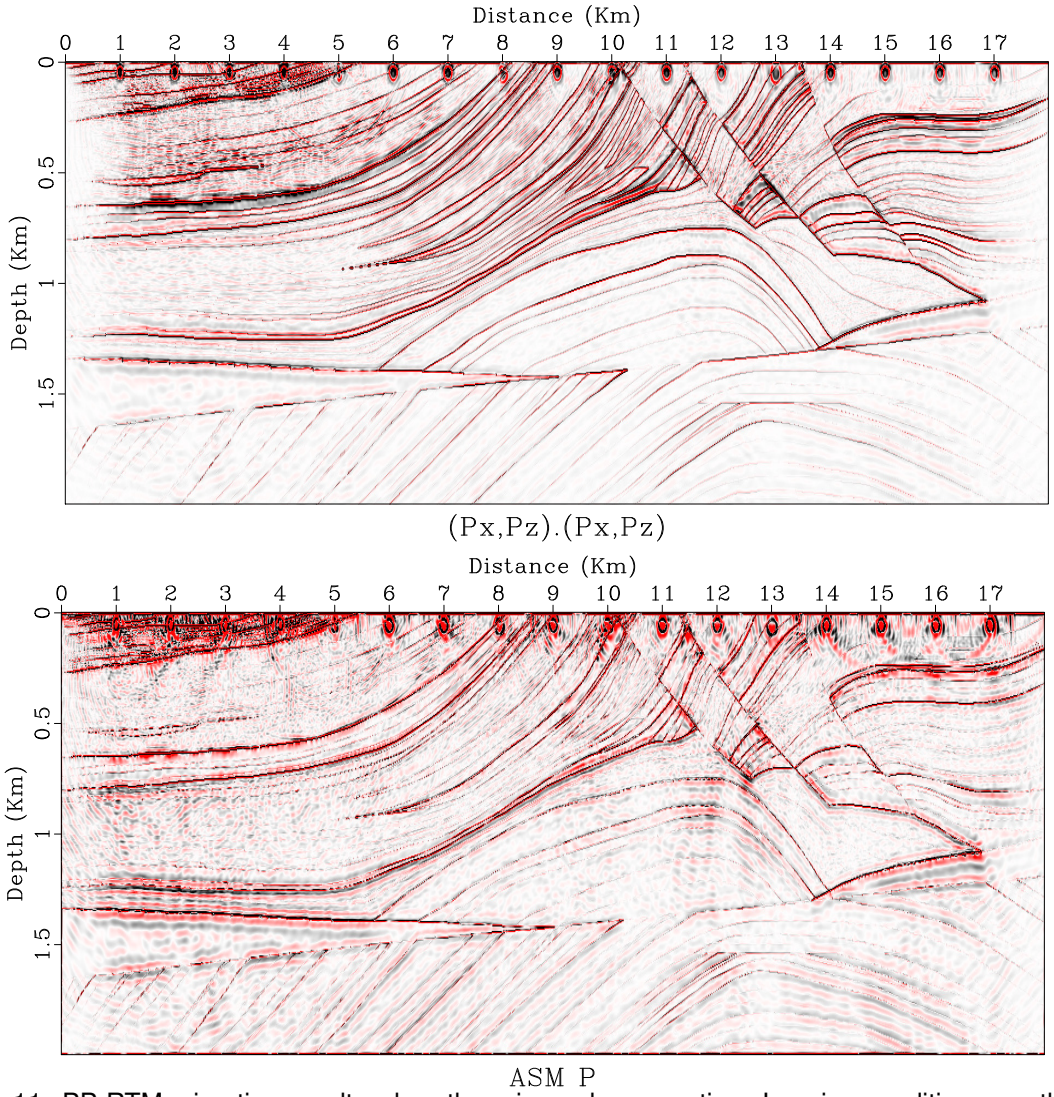

FIG. 11. PP RTM migration results when there is mode separation. Imaging conditions are those of equations 7 and 10. From top to bottom they are P dot product and adjoint state method P.

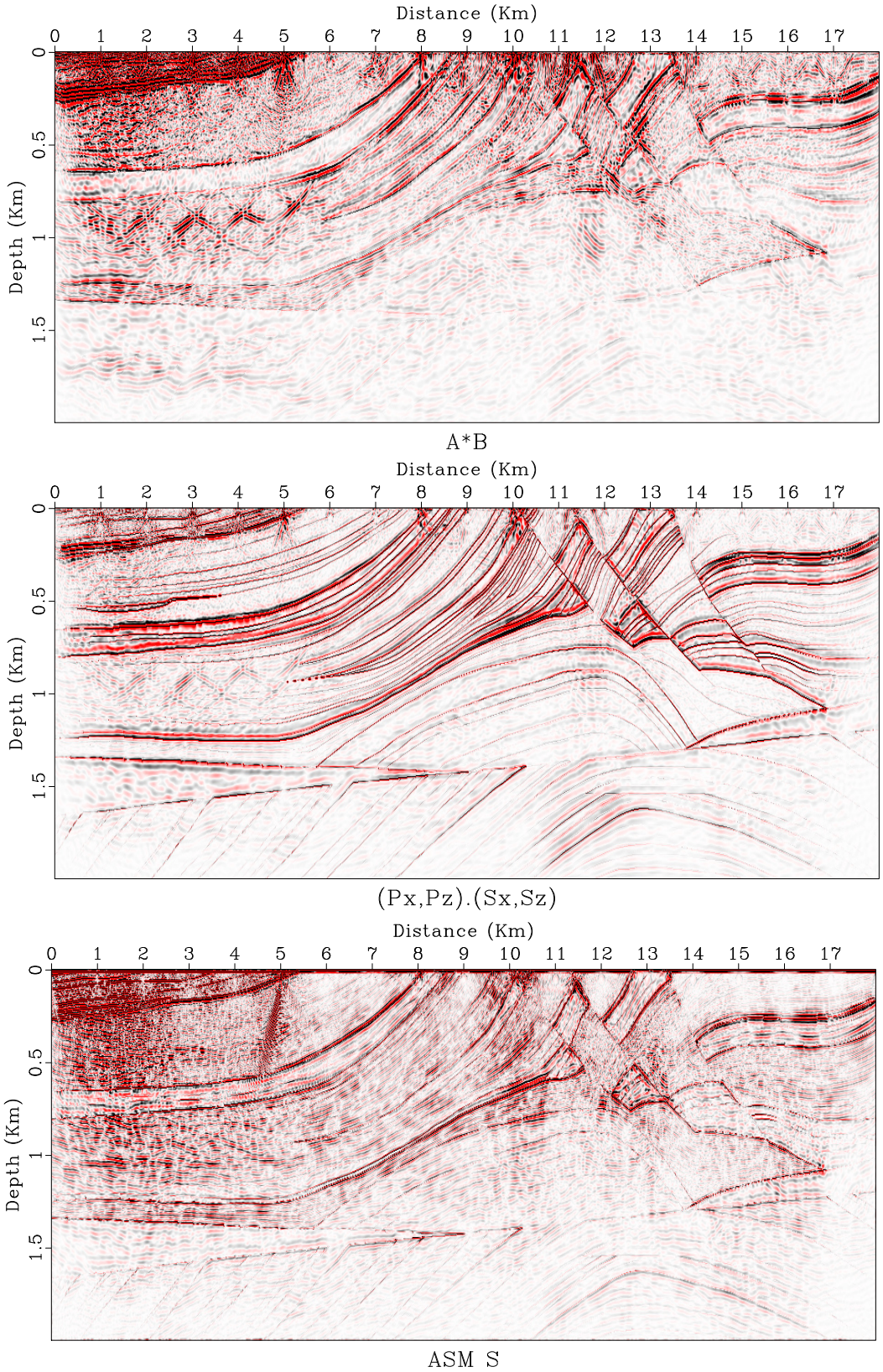

FIG. 12. PS RTM migration results when there is mode separation. Imaging conditions are those of equations 8, 9 and 11. ASM stands for adjoint state method. From top to bottom they are A times B, PS dot product and adjoint state method S.

adjoint of the Born operator that is applied in demigration. Their main objective is to be used as an approximation of the gradient in least squares RTM. Although they were not designed with the purpose of improving the seismic image, it is reassuring that these imaging conditions come from a well established theory.

The problem of the polarity reversal seems trivial because it could be solved by just flipping one half of the horizontal seismograms, as is usually done in practice. However, this only works when the normal incidence is vertical. As mentioned before, two of the pure P- and S-wave PS imaging conditions do not show this reversal. The explanation is that these imaging conditions always cross-correlate pairs of wavefields when the reversal is present or absent in both. For example, B have the reversal but its horizontal derivative does not and is cross-correlated with v_{sz} that do not have the reversal too.

However, as mentioned in the introduction, the PP dot product imaging condition creates a polarity reversal when the angle of incidence is greater that $45°$. We tried to create this effect with synthetic data, but we were unable. Besides, none of the proposed imaging conditions correct this issue.

As mentioned before, the near surface acts as a wave mode filter that makes most of the P-waves go to the vertical geophone and most of the S-waves go to the horizontal ones. It is possible that without this filter effect the imaging conditions evaluation tend to lean towards the pure modes RTM.

The input data for the pure P- and S-wave RTM must be P- and S-wave seismograms. This means that the normal vertical and horizontal particle or velocity seismograms should be separated. Separating vertical and horizontal displacements is easy when you have the whole wavefields and the depth dimension, but seismograms are recorded in time. However, some authors like Gong et al. (2018) have addressed this issue.

We regard the adjoint state method imaging conditions as PP and PS imaging conditions because the source used in the experiments was P-wave. As mentioned before, these imaging conditions were gradient of a least squares RTM objective function with respect to P- and S-wave velocities, respectively.

CONCLUSIONS

Regarding the pure P- and S-wave RTM imaging conditions, the PP and PS dot product generated the best images. These imaging conditions were reported before in (Du et al., 2017) but they use a different finite difference system.

The adjoint state imaging conditions were second place. However, they performed much better than the classical non-pure modes imaging conditions and they do not suffer from PS polarity reversal. PP polarity reversal is still unknown.

To be fair, regarding the non-pure modes RTM imaging conditions, the sum of stresses

and the divergence also produced very good migrated images. Although they are limited to only PP imaging.

FUTURE WORK

We are very interested in applying the PP and PS imaging conditions to real data. We think they could be useful when delineating changes produced by CO2 storage. Actually, there is a facility near Brooks where C02 is going to be injected and multicomponent conventional and DAS seismic monitoring equipment is already installed. Some of the monitoring is from a VSP survey, so we also want to accommodate the algorithms to this survey geometry.

We want to implement the technique mentioned earlier to turn conventional multicomponent seismograms into pure P- and S-waves seismograms. There is room for improvement since this problem is still open.

We are going to delve more into the PP reversal problem mentioned in the literature. As mentioned before, we still cannot produce it in our synthetic experiments.

Some modelling with the near surface included could show the real potential of the cross-correlations between Cartesian components.

As stated earlier, the imaging conditions based on the adjoint state method are the gradient of a least squares RTM. We have the aim to use them in that kind of migration technology.

ACKNOWLEDGEMENTS

We would like to express our gratitude to the sponsors of CREWES for continued support. This work was funded by CREWES industrial sponsors and NSERC (Natural Science and Engineering Research Council of Canada).

REFERENCES

Alves, G., and Biondi, B., 2016, Imaging condition for elastic reverse time migration, 4173–4177.

Balch, A., and Erdemir, C., 1994, Sign-change correction for prestack migration of p-s converted wave reflections: Geophysical Prospecting, **42**, No. 6, 637–663.

Baysal, E., Kosloff, D. D., and Sherwood, J. W. C., 1983, Reverse time migration: GEOPHYSICS, **48**, No. 11, 1514–1524.

Berenger, J.-P., 1994, A perfectly matched layer for the absorption of electromagnetic waves: Journal of Computational Physics, **114**, No. 2, 185 – 200.

Chang, W., and McMechan, G. A., 1994, 3-d elastic prestack, reverse time depth migration: GEOPHYSICS, **59**, No. 4, 597–609.

Chen, K.-Y., 2014, Finite-difference simulation of elastic wave with separation in pure p- and s-modes: Journal of Computational Methods in Physics, 14.

Claerbout, J. F., 1971, Toward a unified theory of reflector mapping: GEOPHYSICS, **36**, No. 3, 467–481.

Du, Q., Guo, C., Zhao, Q., Gong, X., Wang, C., and yang Li, X., 2017, Vector-based elastic reverse time migration based on scalar imaging condition: GEOPHYSICS, **82**, No. 2, S111–S127.

Du, Q., Zhu, Y., and Ba, J., 2012, Polarity reversal correction for elastic reverse time migration: GEOPHYSICS, **77**, No. 2, S31–S41.

Duan, Y., and Sava, P., 2015, Scalar imaging condition for elastic reverse time migration: GEOPHYSICS, **80**, No. 4, S127–S136.

Feng, Z., and Schuster, G. T., 2017, Elastic least-squares reverse time migration: GEOPHYSICS, **82**, No. 2, S143–S157.

Gong, X., Du, Q., Zhao, Q., Sun, P., Zhang, J., and Tian, Z., 2018, Elastic wave-equation datuming: GEOPHYSICS, **83**, No. 5, U51–U61.

Gu, B., Li, Z., Ma, X., and Liang, G., 2015, Multi-component elastic reverse time migration based on the p- and s-wave separated velocity-stress equations: Journal of Applied Geophysics, **112**, 62 – 78.

H. Khaniani, S. M., and Trad, D., 2017, A (full) waveform inversion based on pure p- and s- wave separation, Tech. rep., CREWES.

Jiang, Z., 2012, Elastic wave modelling and reverse-time migration by a staggered-grid finite-difference method: Ph.D. thesis, Unversity of Calgary.

Levander, A. R., 1988, Fourth-order finite-difference p-sv seismograms: GEOPHYSICS, **53**, No. 11, 1425–1436.

Ma, D., and Zhu, G., 2003, Numerical modeling of p-wave and s-wave separation in elastic wavefield: Shiyou Diqiu Wuli Kantan/Oil Geophysical Prospecting, **38**, No. 5, 482.

McMechan, G. A., 1983, Migration by extrapolation of time-dependent boundary values: Geophysical Prospecting, **31**, No. 3, 413–420.

Nguyen, B. D., and McMechan, G. A., 2015, Five ways to avoid storing source wavefield snapshots in 2d elastic prestack reverse time migration: GEOPHYSICS, **80**, No. 1, S1–S18.

Rocha, D., Tanushev, N., and Sava, P., 2016, Isotropic elastic wavefield imaging using the energy norm: GEOPHYSICS, **81**, No. 4, S207–S219.

Sava, P., and Hill, S. J., 2009, Overview and classification of wavefield seismic imaging methods: The Leading Edge, **28**, No. 2, 170–183.

Schuster, G., 2017, Seismic Inversion: Society of Exploration Geophysicists.

Sun, R., and McMechan, G. A., 2001, Scalar reverse time depth migration of prestack elastic seismic data: GEOPHYSICS, **66**, No. 5, 1519–1527.

Versteeg, R., 1994, The marmousi experience: Velocity model determination on a synthetic complex data set: The Leading Edge, **13**, No. 9, 927–936.

Wang, W., and McMechan, G. A., 2015, Vector-based elastic reverse time migration: GEOPHYSICS, **80**, No. 6, S245–S258.

Whitmore, N. D., 1983, Iterative depth migration by backward time propagation, 382–385.

Yan, J., and Sava, P., 2008, Isotropic angle-domain elastic reverse-time migration: GEOPHYSICS, **73**, No. 6, S229–S239.

Zhang, S., Du, Q., and Zhang, X., 2018, Vector-based second-order divergence imaging condition for elastic reverse time migration, 4443–4447.

Zhu, H., Luo, Y., Nissen-Meyer, T., Morency, C., and Tromp, J., 2009, Elastic imaging and time-lapse migration based on adjoint methods: GEOPHYSICS, **74**, No. 6, WCA167–WCA177.

APPENDIX

Adjoint state method imaging condition derivation

Following Feng and Schuster (2017), we can express the pure P- and S-wave system of equations 1 as a matrix operator $\boldsymbol{S}$:

$$\begin{pmatrix} \frac{\partial}{\partial t} & 0 & 0 & 0 & -\alpha^2\frac{\partial}{\partial x} & 0 \\ 0 & \frac{\partial}{\partial t} & 0 & 0 & -\alpha^2\frac{\partial}{\partial z} & 0 \\ 0 & 0 & \frac{\partial}{\partial t} & 0 & 0 & -\beta^2\frac{\partial}{\partial z} \\ 0 & 0 & 0 & \frac{\partial}{\partial t} & 0 & \beta^2\frac{\partial}{\partial x} \\ -\frac{\partial}{\partial x} & -\frac{\partial}{\partial z} & -\frac{\partial}{\partial x} & -\frac{\partial}{\partial z} & \frac{\partial}{\partial t} & 0 \\ -\frac{\partial}{\partial z} & \frac{\partial}{\partial x} & -\frac{\partial}{\partial z} & \frac{\partial}{\partial x} & 0 & \frac{\partial}{\partial t} \end{pmatrix} \begin{pmatrix} v_{px} \\ v_{pz} \\ v_{sx} \\ v_{sz} \\ A \\ B \end{pmatrix} = \begin{pmatrix} 0 \\ 0 \\ 0 \\ 0 \\ f_A \\ f_B \end{pmatrix}$$

$$\boldsymbol{S}\boldsymbol{w} = \boldsymbol{F}$$

The adjoint state method proclaims the following expression for the elastic least squares RTM migration gradient with respect to the model parameters $\boldsymbol{m} = [\alpha, \beta]^T$:

$$\frac{\partial \epsilon}{\partial \boldsymbol{m}} = -\langle \frac{\partial \boldsymbol{S}}{\partial \boldsymbol{m}}\boldsymbol{w}, (\boldsymbol{S}^{-1})^* \Delta \boldsymbol{d} \rangle,$$

where ϵ is the elastic least squares RTM objective function and $\Delta \boldsymbol{d}$ are the shot gathers. The second element of the dot product could be seen as a backward wave propagation using the adjoint operator $\boldsymbol{S}^*$ and the shot gathers as sources:

$$\begin{aligned}
\frac{\partial \epsilon}{\partial \boldsymbol{m}} &= -\langle \frac{\partial \boldsymbol{S}}{\partial \boldsymbol{m}} \boldsymbol{w}, \boldsymbol{w}^* \rangle \\
\boldsymbol{w}^* &= (\boldsymbol{S}^{-1})^* \Delta \boldsymbol{d} \\
\boldsymbol{S}^* \boldsymbol{w}^* &= \Delta \boldsymbol{d} \\
\boldsymbol{w}^* &= [\hat{v}_{px}, \hat{v}_{pz}, \hat{v}_{sx}, \hat{v}_{sz}, \hat{A}, \hat{B}]^T
\end{aligned} \tag{12}$$

where vector $\boldsymbol{w}^*$ contains the adjoint wavefields. They can be obtained by implementing this system using finite differences. The especific expressions for the dot products in equation 12 can be calculated in the following way for the two gradient vector components $\frac{\partial \epsilon}{\partial \boldsymbol{m}} = \left[\frac{\partial \epsilon}{\partial \alpha}, \frac{\partial \epsilon}{\partial \beta}\right]^T$:

$$\begin{aligned}
\frac{\partial \epsilon}{\partial \alpha} &= -\langle \frac{\partial}{\partial \alpha} \begin{pmatrix} \frac{\partial}{\partial t} & 0 & 0 & 0 & -\alpha^2 \frac{\partial}{\partial x} & 0 \\ 0 & \frac{\partial}{\partial t} & 0 & 0 & -\alpha^2 \frac{\partial}{\partial z} & 0 \\ 0 & 0 & \frac{\partial}{\partial t} & 0 & 0 & -\beta^2 \frac{\partial}{\partial z} \\ 0 & 0 & 0 & \frac{\partial}{\partial t} & 0 & \beta^2 \frac{\partial}{\partial x} \\ -\frac{\partial}{\partial x} & -\frac{\partial}{\partial z} & -\frac{\partial}{\partial x} & -\frac{\partial}{\partial z} & \frac{\partial}{\partial t} & 0 \\ -\frac{\partial}{\partial z} & \frac{\partial}{\partial x} & -\frac{\partial}{\partial z} & \frac{\partial}{\partial x} & 0 & \frac{\partial}{\partial t} \end{pmatrix} \begin{pmatrix} v_{px} \\ v_{pz} \\ v_{sx} \\ v_{sz} \\ A \\ B \end{pmatrix}, \begin{pmatrix} \hat{v}_{px} \\ \hat{v}_{pz} \\ \hat{v}_{sx} \\ \hat{v}_{sz} \\ \hat{A} \\ \hat{B} \end{pmatrix} \rangle \\
&= -\langle \begin{pmatrix} 0 & 0 & 0 & 0 & -2\alpha \frac{\partial}{\partial x} & 0 \\ 0 & 0 & 0 & 0 & -2\alpha \frac{\partial}{\partial z} & 0 \\ 0 & 0 & 0 & 0 & 0 & 0 \\ 0 & 0 & 0 & 0 & 0 & 0 \\ 0 & 0 & 0 & 0 & 0 & 0 \\ 0 & 0 & 0 & 0 & 0 & 0 \end{pmatrix} \begin{pmatrix} v_{px} \\ v_{pz} \\ v_{sx} \\ v_{sz} \\ A \\ B \end{pmatrix}, \begin{pmatrix} \hat{v}_{px} \\ \hat{v}_{pz} \\ \hat{v}_{sx} \\ \hat{v}_{sz} \\ \hat{A} \\ \hat{B} \end{pmatrix} \rangle \\
&= 2\alpha \left(\frac{\partial A}{\partial x} \hat{v}_{px} + \frac{\partial A}{\partial z} \hat{v}_{pz} \right)
\end{aligned}$$

$$\begin{aligned}
\frac{\partial \epsilon}{\partial \beta} &= -\langle \frac{\partial}{\partial \beta} \begin{pmatrix} \frac{\partial}{\partial t} & 0 & 0 & 0 & -\alpha^2 \frac{\partial}{\partial x} & 0 \\ 0 & \frac{\partial}{\partial t} & 0 & 0 & -\alpha^2 \frac{\partial}{\partial z} & 0 \\ 0 & 0 & \frac{\partial}{\partial t} & 0 & 0 & -\beta^2 \frac{\partial}{\partial z} \\ 0 & 0 & 0 & \frac{\partial}{\partial t} & 0 & \beta^2 \frac{\partial}{\partial x} \\ -\frac{\partial}{\partial x} & -\frac{\partial}{\partial z} & -\frac{\partial}{\partial x} & -\frac{\partial}{\partial z} & \frac{\partial}{\partial t} & 0 \\ -\frac{\partial}{\partial z} & \frac{\partial}{\partial x} & -\frac{\partial}{\partial z} & \frac{\partial}{\partial x} & 0 & \frac{\partial}{\partial t} \end{pmatrix} \begin{pmatrix} v_{px} \\ v_{pz} \\ v_{sx} \\ v_{sz} \\ A \\ B \end{pmatrix}, \begin{pmatrix} \hat{v}_{px} \\ \hat{v}_{pz} \\ \hat{v}_{sx} \\ \hat{v}_{sz} \\ \hat{A} \\ \hat{B} \end{pmatrix} \rangle \\
&= -\langle \begin{pmatrix} 0 & 0 & 0 & 0 & 0 & 0 \\ 0 & 0 & 0 & 0 & 0 & 0 \\ 0 & 0 & 0 & 0 & 0 & -2\beta \frac{\partial}{\partial z} \\ 0 & 0 & 0 & 0 & 0 & 2\beta \frac{\partial}{\partial x} \\ 0 & 0 & 0 & 0 & 0 & 0 \\ 0 & 0 & 0 & 0 & 0 & 0 \end{pmatrix} \begin{pmatrix} v_{px} \\ v_{pz} \\ v_{sx} \\ v_{sz} \\ A \\ B \end{pmatrix}, \begin{pmatrix} \hat{v}_{px} \\ \hat{v}_{pz} \\ \hat{v}_{sx} \\ \hat{v}_{sz} \\ \hat{A} \\ \hat{B} \end{pmatrix} \rangle \\
&= 2\beta \left(\frac{\partial B}{\partial z} \hat{v}_{sx} - \frac{\partial B}{\partial x} \hat{v}_{sz} \right)
\end{aligned}$$

Something to notice is that the derivative with respect to P-wave particle velocity α only involves P-wave velocity and A wavefields, while the derivative with respect to S-wave velocity β only includes S-wave particle velocity and B wavefields.

Adjoint state method imaging condition in three dimensions

H. Khaniani and Trad (2017) show the complete 3-D version of the pure P- and S- wave system of equations 1. Using this system and following the same methodology of the last section, the 3-D adjoint state method imaging conditions are:

$$
\begin{aligned}
I_{PP} &= 2\alpha \int_0^T \left(\frac{\partial A}{\partial x}, \frac{\partial A}{\partial y}, \frac{\partial A}{\partial z} \right) \cdot (\hat{v}_{px}, \hat{v}_{py}, \hat{v}_{pz}) dt \\
I_{PS} &= 2\beta \int_0^T \left(\frac{\partial B_2}{\partial z} + \frac{\partial B_3}{\partial y}, -\frac{\partial B_3}{\partial x} - \frac{\partial B_1}{\partial z}, \frac{\partial B_1}{\partial y} + \frac{\partial B_2}{\partial x} \right) \cdot (\hat{v}_{sx}, \hat{v}_{sy}, \hat{v}_{sz}) dt
\end{aligned}
$$